

Improving solar wind forecasting using Data Assimilation

Matthew Lang ¹, Jake Witherington ¹, Harriet Turner ¹, Mathew J. Owens ¹,
Pete Riley ²

¹Department of Meteorology, University of Reading, Reading, Berkshire, UK

²Predictive Science Inc., 9990 Mesa Rim Rd., Suite 170, San Diego, CA, 92121, USA

Key Points:

- This paper shows solar wind forecast improvements from using data assimilation (DA) from 2007-2014.
- Initialising forecasts with DA leads to a 31.4% reduction in RMSEs compared to forecasts with no DA.
- DA can remove significant positive correlations between forecast RMSE and latitude of STEREO B

Abstract

Data Assimilation (DA) has enabled huge improvements in the skill of terrestrial operational weather forecasting. In this study, we use a variational DA scheme with a computationally efficient solar wind model and in situ observations from STEREO A, STEREO B and ACE. This scheme enables solar-wind observations far from the Sun, such as at 1 AU, to update and improve the inner boundary conditions of the solar wind model (at 30 solar radii). In this way, observational information can be used to improve estimates of the near-Earth solar wind, even when the observations are not directly downstream of the Earth. This allows improved initial conditions of the solar wind to be passed into forecasting models. To this effect we employ the HUXt solar wind model to produce 27-day forecasts of the solar wind during the operational time of STEREO B (01/11/2007–30/09/2014). At ACE, we compare these DA forecasts to the corotation of STEREO B observations and find that 27-day RMSE for STEREO-B corotation and DA forecasts are comparable. However, the DA forecast is shown to improve solar wind forecasts when STEREO-B’s latitude is offset from Earth. And the DA scheme enables the representation of the solar wind in the whole model domain between the Sun and the Earth to be improved, which will enable improved forecasting of CME arrival time and speed.

1 Introduction

The solar wind is a continuous outflow of plasma and magnetic flux which fills the heliosphere (e.g., *Owens and Forsyth* [2013]). Variations in the solar wind properties in near-Earth space can lead to adverse effects [*Hapgood*, 2011], such as disruption to power and communications systems, and health hazards for astronauts and aircrew on flights over the poles. As a result, it is vital to forecast the solar wind accurately and efficiently. However, forecasting ahead by more than about one hour (the nominal time it takes for the solar wind to travel from $L1$ to Earth) requires prediction of the solar wind conditions near the Sun. This is typically achieved using empirical relations to the coronal magnetic field [*Arge et al.*, 2003; *McGregor et al.*, 2011; *Riley et al.*, 2015], which is in turn determined using extrapolation from the observed photospheric magnetic field [*Mackay and Yeates*, 2012; *Linker et al.*, 1999]. These empirical models approximate the solar wind conditions at $\sim 21 - 30$ solar radii (r_S). From here, the solar wind is propagated to Earth, typically using a numerical magnetohydrodynamic (MHD) model, such as Enlil [*Odstrcil*, 2003], HelioMAS [*Riley et al.*, 2012] or EUHFORIA [*Poedts and Pomoell*, 2017], with no further observational constraints.

In this study, however, we apply a further step using Data Assimilation (DA), by assimilating in-situ observations of the solar wind, before forecasting the solar wind. Data assimilation is the process by which observational data is incorporated into numerical models to improve knowledge of the trajectory, and uncertainties, of the model state. In operational meteorological models, data assimilation is commonly used to generate an optimal initial state to be used in subsequent forecasts through the use of prior knowledge of the state (e.g. a previous forecast) and observational data obtained from satellites/weather stations etc. Data assimilation is considered a vital step in meteorological forecasting, reducing the impact of the ‘butterfly effect’ (where small changes in initial conditions lead to large differences in model evolution), and hence improving the forecasting skill. Improvements in numerical weather predictions have gone hand-in-hand with improvements in the implementation of the observation network and data assimilation methods into the models. This has led to huge improvements in the lead-times over which forecasts are accurate [*Kalnay*, 2003]. This can clearly be seen in Figure 1. In the late nineties, a significant improvement was made to data assimilation methodology (3DVar was upgraded to 4DVar) and satellite observations were included in the data assimilation, vastly increasing observational

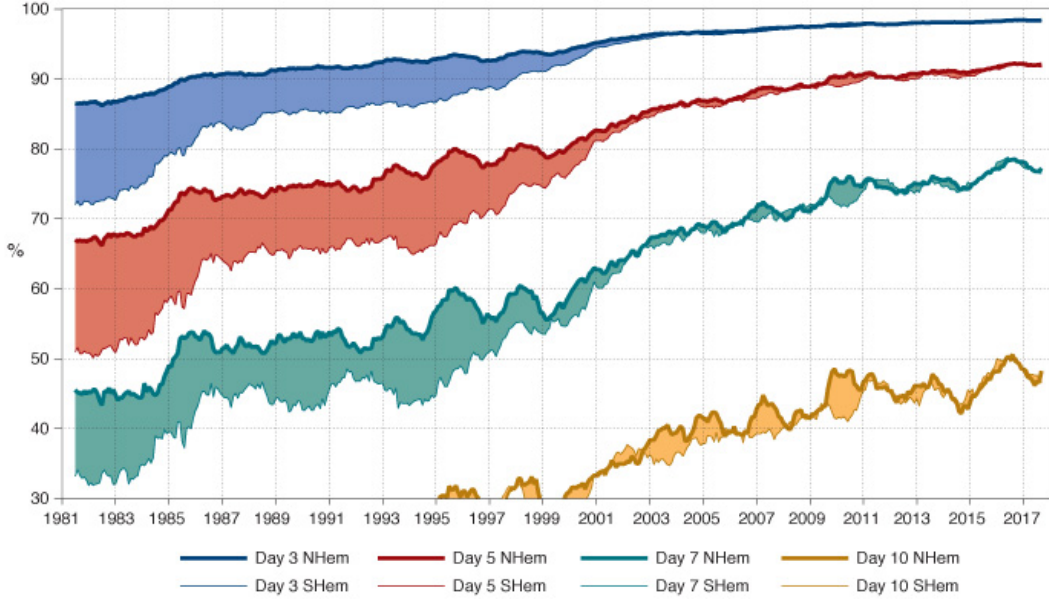


Figure 1: The 12-month running mean of the anomaly correlation for ECMWF’s 500hPa geopotential height forecasts in the northern and the southern hemisphere at 3–day (blue), 5–day (red), 7–day (green) and 10–day (yellow) lead-times. The shaded regions show the difference between the northern (top) and southern (bottom) hemispheres, which is largely a result of differing observational coverage.

coverage. The assimilation of satellite observations led to vast improvements in Southern Hemisphere forecasts especially, leading to the closing of the gap in Northern and Southern Hemisphere forecast skill. Space weather forecasting has not yet exploited the full potential available from implementing data assimilation methods in forecasting models.

In space-weather forecasting, data assimilation has been attempted in three main domains: the photosphere, the solar wind and the ionosphere. Ionospheric data assimilation is arguably the most mature, owing to the relatively good observational coverage. Various DA methodologies have been applied to the ionosphere, such as 3DVar [Bust and Mitchell, 2008], 4DVar [Wang *et al.*, 2004] and the Local Ensemble Transform Kalman Filter (LETKF) [Durazo *et al.*, 2017]. Photospheric data assimilation, such as the Air Force Data Assimilative Photospheric Flux Transport (ADAPT) model [Arge *et al.*, 2010], uses observations of the magnetic field at the Sun’s surface with physics-based temporal evolution to improve the inner boundary condition to coronal models. The resulting representation of the corona can in turn be used to generate new inner-boundary conditions for solar wind models. In solar wind applications, data assimilation of in-situ observations of the solar wind has been shown to lead to improvements in estimates of the solar wind state; Lang *et al.* [2017] used the LETKF to improve the representation of the modelled solar wind, the first implementation of complex DA methodologies into the solar wind system. Whilst parallel computing has meant that ensemble-based methods are relatively easy to implement for complex numerical models [Browne and Wilson, 2015; Nerger *et al.*, 2005], the LETKF was unable to map information back towards the Sun. Thus any improvements made by the DA are swept radially away from the observation point by the ambient solar wind. Thus without in-situ observations upstream of the point of interest, which for Earth is rare, little forecast improvement is expected. Lang and Owens [2019] generated a

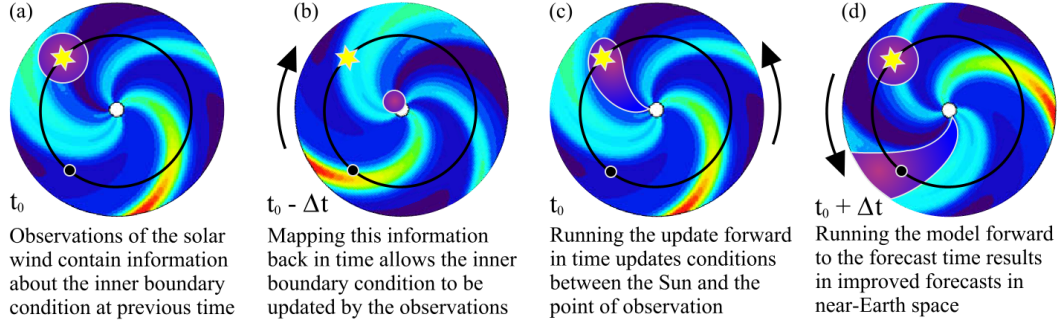


Figure 2: A schematic giving an overview of how the BRAVDA scheme works.

variational data assimilation scheme with a simple solar wind propagation model (see *Riley et al.* [2012] and *Owens and Riley* [2017] for more details) that could map information from in-situ observation point at near-Earth orbit to the inner solar wind model boundary. This was shown to give improved and persistent updates to the solar wind over a 27-day period. However, this demonstration of improved solar wind reconstruction was not directly analogous to how the method would work in a forecast situation.

In this study, we investigate how data assimilation of in-situ observations affects solar wind forecast (strictly speaking, hindcast) skill. We will use the Burger Radial Variational Data Assimilation (BRAVDA) scheme that was developed in *Lang and Owens* [2019] to assimilate observations from Solar-Terrestrial Relations Observatory (STEREO) [*Kaiser et al.*, 2008] spacecraft and the Advanced Composition Explorer (ACE) [*Stone et al.*, 1998]. The BRAVDA scheme will be used to generate 27-day reanalysis sets over the operational lifetime of the STEREO-B satellite (01/11/2007-30/09/2014). For each 27-day DA analysis, a 27-day solar wind forecast will be produced using the HUXt (Heliospheric Upwind Extrapolation with time dependence) solar wind forecasting model [*Owens et al.*, 2020a], initialised with the results of the BRAVDA scheme. These forecasts will be presented and their accuracy will be verified against in-situ observations at STEREO and ACE. As a benchmark, a STEREO-B corotation forecast will also be produced (where available) at L1 for comparison with ACE observations. To produce this corotation forecast, the Sun will be assumed to be steady and the solar wind is assumed to statically rotate with the Sun. Therefore, the observations at STEREO-B are predicted to be the solar wind conditions at L1 x time later, where x is the time it takes for the Sun to rotate from STEREO-B to L1 [*Thomas et al.*, 2018; *Kohutova et al.*, 2016].

This paper will describe the BRAVDA scheme and the HUXt forecasting model. Numerical experiments will then be presented, analysing the 7-year BRAVDA reanalyses and subsequent HUXt forecasts. Statistical analysis shall be performed and the improvements due to data assimilation will be discussed. In the final section, we shall make conclusions and discuss future developments.

2 The BRAVDA system

The BRAVDA scheme is a variational data assimilation scheme *Lang and Owens* [2019], to map information from in-situ observations, typically near 1 AU, back to a solar wind model's inner boundary (in this case, 30 solar radii (r_S)). Figure 2 outlines quantitatively how the BRAVDA scheme works: our current estimate for the solar wind speed at the inner boundary is mapped out to the observation radius using our solar wind propagation model. Information from the observation (including its uncertainty)

is then mapped back towards the Sun (Figure 2a-2b), where it is used to update the inner boundary of the solar wind model. The updated inner boundary is propagated back out using the solar wind model (Figure 2c), the results of which can then be used to produce forecasts of the solar wind speed at Earth (Figure 2d).

The solar wind model used by BRaVDA is based upon a solar wind speed propagation model, developed by *Riley and Lionello* [2011], which maps the (two-dimensional) equatorial solar wind speed over the heliocentric domain from $30r_S$ to $236r_S$ from the Sun:

$$v_{i+1,j}(\phi) = v_{i,j} + \frac{\Delta r \Omega_{ROT}}{v_{i,j}} \left(\frac{v_{i,j+1} - v_{i,j}}{C \Delta \phi} \right) \quad (1)$$

where $v_{i,j}$ is the speed (in km/s) at radius, r_i (the i is the radius coordinate), and at Carrington longitude, ϕ_j (where j is the longitude coordinate). Using the same setup as *Owens and Riley* [2017], $\Delta r = 1.4853r_S$ is the radial grid resolution (in km), $\Delta \phi = 2.81^\circ$ is the longitudinal grid resolution, $C = \frac{2\pi}{180}$ is a constant representing the conversion factor from degrees to radians and $\Omega_{ROT} = \frac{2\pi}{25.38(86400)} s^{-1}$ is the solar rotational speed.

After this solution is obtained, an additional term, $v_{i,j}^{acc}$, is added to the $v_{i,j}$ to represent the acceleration of the solar wind in the domain considered, which is given by:

$$v_{i,j}^{acc} = \alpha v_{0,j}(\phi) \left(1 - e^{\frac{r_i}{r_H}} \right) \quad (2)$$

where $v_{0,j}$ is the solar wind speed at the inner-boundary and $\alpha = 0.15$ and $r_H = 50r_S$ are constants determined by *Riley and Lionello* [2011].

Given the 2-dimensional nature of this solar wind propagation model, we only represent a single heliolatitude. In reality there is typically a latitudinal off set between observing spacecraft and the desired forecast location. For example, the STEREO spacecraft are in the ecliptic plane, which is inclined by 7.25° to the heliographic equator. A solar wind DA scheme in a full 3-dimensional solar wind model could relax this assumption, though the problem of determining the latitudinal representivity of the observations remains.

In data assimilation, we aim to construct the true state vector, \mathbf{x}^t , an N_x -dimensional vector that contains the values of the quantities of interest at all gridpoints from prior knowledge about the system (e.g. a previous forecast) and observations, \mathbf{y} . The variables within a state vector for meteorological applications can include the precipitation over Africa, the mean sea level pressure over France, wind speed/direction in Llanfairpwllgwyngyllgogerychwyrndrobwilllantysiliogogogoch etc. depending upon the purpose of the numerical model. In the BRaVDA system, the state vector that we wish to estimate is the solar wind speed at the inner-boundary at all longitudinal points (i.e. a 128-dimension vector where the j^{th} entry is equal to $v_{0,j}$).

In order to do this, the errors in the prior and observational information is typically assumed to be normally distributed and the numerical model is assumed to be linear. Using these assumptions, a cost function is constructed based upon the probability distributions of the prior information and the observations, the minimum of which yields the state that maximises the posterior distribution (the probability distribution of the state given the observations, $p(\mathbf{x}|\mathbf{y})$). The BRaVDA scheme also makes an additional assumption that the numerical model is perfect (i.e. the numerical model contains no errors), this typically produces a poorer result than a system that allows for model error, however incorporating model error is an extremely complex operation [*Evensen et al.*, 1998; *Lang et al.*, 2016], and is well beyond the scope of this

study. The BRaVDA Cost Function to be minimised, $\mathcal{J}(\mathbf{x}_0)$, is given by:

$$\mathcal{J}(\mathbf{x}_0) = \frac{1}{2}(\mathbf{x}_0 - \mathbf{x}^b)^T \mathbf{B}^{-1}(\mathbf{x}_0 - \mathbf{x}^b) + \frac{1}{2} \sum_{k=0}^{N_y} [(\mathbf{y}_k - \mathcal{H}_k(\mathbf{x}_0)) \mathbf{R}_k^{-1}(\mathbf{y}_k - \mathcal{H}_k(\mathbf{x}_0))] \quad (3)$$

where \mathbf{x}_0 is the state at the initial time; \mathbf{x}^b is the prior state generated from prior information about the system (e.g. from a previous forecast); \mathbf{B} is the prior error covariance matrix that defines the uncertainty in the prior state; \mathbf{y}_k is the k^{th} observation; \mathcal{H}_k is known as the observation operator and is a function that maps the state to the observation space (i.e. $\mathcal{H}_k(\mathbf{x}_0)$ tells us what the numerical model ‘thinks’ the observation should be); \mathbf{R}_k is the observation error covariance matrix and N_y is the number of observations. The full derivation of this cost function can be found in Appendix A of ?.

The cost function is the sum of the relative contributions of the errors present within the solar wind system. The first term in the cost function represents the prior errors, $(\mathbf{x}_0 - \mathbf{x}_0^b)$, weighted by the prior error covariance matrix, \mathbf{B}^{-1} . The second term represents the sum of the observation errors, $(\mathbf{y}_k - \mathcal{H}_k[f_{r_k-1}(f_{r_k-2}(\dots f_0(\mathbf{v}_0)\dots))])$, and is weighted by the observation error covariance matrix \mathbf{R}_k^{-1} . Therefore, the optimal state, that minimises the errors in the system, is the state that minimises the cost function. The weighting by the inverse of the error covariance matrices means that if there is a high amount of certainty in, for example, the prior state compared to that of the observations, then \mathbf{B}^{-1} will be much larger than \mathbf{R}^{-1} , meaning that the optimal state vector will have to move closer to the prior state to minimise the cost function, increasing the dominance of the prior state on the final analysis.

In principle, the DA framework shown here is also applicable to other solar wind observations, such as Interplanetary Scintillation (IPS; e.g., *Breen et al.* [2006]) or Heliospheric Imagers (HI; e.g., *Eyles et al.* [2009]). These remote measurements of solar wind density structures are subject to line-of-sight integration effects, and estimation of solar wind speed further requires some form of correlation tracking. Thus relative to (single-point) in-situ observations, there is increased uncertainty in both the measurement and its location, but with the advantage of a more synoptic picture of the solar wind. By explicitly accounting for observational errors, a solar wind DA scheme can exploit the positives of both forms of data. Though accurately determining the observational errors is a significant task which is not addressed in the current study.

3 The HUXt solar wind model

The HUXt (Heliospheric Upwind eXtrapolation with time dependence) solar wind model [*Owens et al.*, 2020a] is a reduced-physics solar wind model based upon Burgers’ inviscid equation.

In order to make the solar-wind model as computationally efficient as possible, a large number of physical assumptions and approximations are required. These approximations include the assumptions that in the heliosphere, pressure gradient and gravitation terms are small compared with the flow momentum and hence can be neglected. A further simplification is that we only consider variations in the radial

direction. These approximations result in the HUXt model equation:

$$\begin{aligned}
 v_i^{n+1} = & v_i^n - v_i^n \frac{\Delta t}{\Delta r} [v_i^n - v_{i-1}^n] \\
 & + v_{i-1}^n \frac{\Delta t}{\Delta r} \alpha v_i^n \left[\frac{A_i}{1 + \alpha A_i} \right] \\
 & - v_{i-1}^n \frac{\Delta t}{\Delta r} \alpha v_{i-1}^n \left[\frac{A_{i-1}}{1 + \alpha A_{i-1}} \right],
 \end{aligned} \tag{4}$$

where v_i^n is the radial speed at radial coordinate i and time coordinate n ; $\Delta r = r_i - r_{i-1}$ and $\Delta t = t^{n+1} - t^n$ are the radial and temporal grid steps, respectively; r_i is the radial distance at radial coordinate i ; t^n is the time at temporal coordinate n and

$$A_j = 1 - \exp \left[\frac{r_0 - r_j}{r_H} \right]. \tag{5}$$

Further details on how this is derived can be found in *Owens et al. [2020a]*.

We use the same radial grid as in *Owens et al. [2020a]*, namely 140 uniformly spaced grid cells between an inner boundary of $30R_S$ and an outer boundary of $236R_S$ and 128 cells equally-spaced longitude grid-points.

For 40+ years of ambient solar-wind solutions, the HUXt model was shown to adequately emulate the full three-dimensional MHD solution to the same $30r_S$ boundary conditions, with solar wind speeds throughout the simulation domain agreeing to within 6%. The biggest difference between the two solutions is that HUXt, by adopting an upwind numerical approach, produces sharper boundaries between slow and fast wind than the MHD solutions.

4 Experimental setup

For BRaVDA method, we must provide a set of conditions in order to proceed. These include specifying the prior error covariance matrix and the observation error covariance matrix, that is the uncertainties in the prior and observation errors respectively. The specification of these conditions is a very important part of the data assimilation process. For example, if the specified prior error uncertainty is too small, the data assimilation analysis will have too much confidence in the quality of the prior state and the data assimilated analysis state will have less freedom to move away from it.

In meteorology, the prior error covariance matrix, \mathbf{B} , is built up by operational centres studying the misfits between forecasts and reanalysis datasets. In comparison, the space weather forecasting is a relatively young science and we do not have this back-catalogue of available forecasting and reanalysis datasets to compare against. As in *Lang and Owens [2019]*, the prior error covariance matrix is approximated using a 576-member ensemble of solar wind speed states, with 15° localisation (see *Lang and Owens [2019]* for more details about localisation), that is generated in the same way as *Owens and Riley [2017]*. Each ensemble member is derived from Carrington rotation solutions of the MAS (Magnetohydrodynamics Around a Sphere) coronal model *Linker et al. [1999]* in which the solar wind speed at $30r_S$ is determined using empirical relations to the coronal magnetic field configuration [*Riley et al., 2012*]. These data are available from <http://www.predsci.com/mhdweb/home.php>.

For each consequent 27-day period from 01/01/2017 – 02/11/2014, the MAS ensemble is extracted for that period and \mathbf{B} is approximated by:

$$\mathbf{B} \approx \frac{1}{M-1} \sum_{m=1}^M \left[\left(\mathbf{v}_0^{(m)} - \overline{\mathbf{v}_0^M} \right) \left(\mathbf{v}_0^{(m)} - \overline{\mathbf{v}_0^M} \right)^T \right] \tag{6}$$

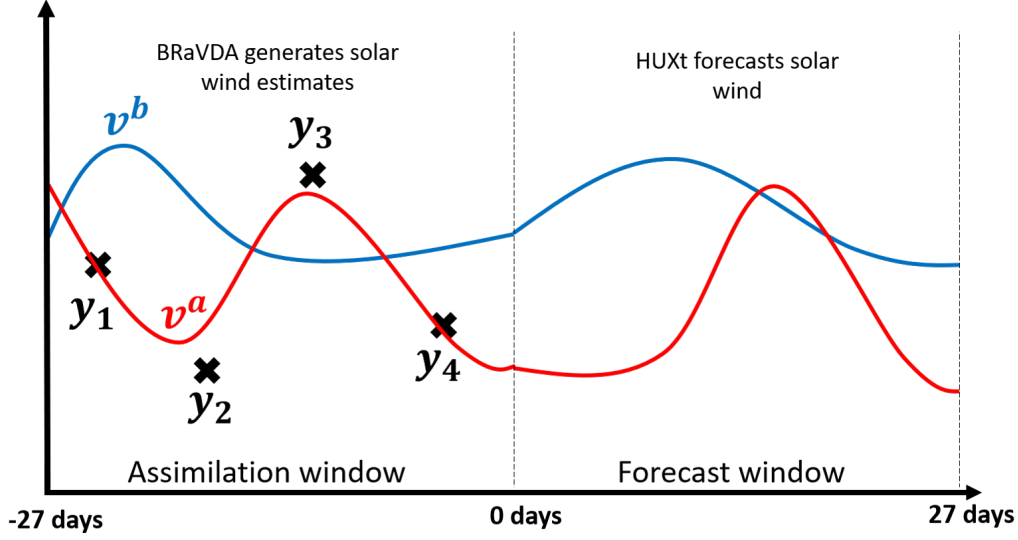


Figure 3: Schematic showing how BRaVDA and HUXt are used to generate solar wind estimates and forecasts. The prior solar wind, \mathbf{v}^b is generated using the radial solar wind propagation scheme defined by equations (1) and (2). The BRaVDA scheme is used to generate an analysis, \mathbf{v}^a , for the 27 days prior to the forecast start-time (the assimilation window). \mathbf{v}^b and \mathbf{v}^a are used to initialise HUXt forecasts of the solar wind speed for the next 27 days (forecast window).

where $\overline{\mathbf{v}_0^M} = \frac{1}{M} \sum_{m=1}^M [v_0^{(m)}]$ and $M = 576$. This is a common technique that is used to approximate uncertainties and a key component of the Ensemble Kalman Filter (EnKF) *Pereira et al.* [2006]. For each 27-day period, the prior initial solar wind speed, \mathbf{v}^b , is randomly drawn from the normal distribution defined by $\mathcal{N}(\overline{\mathbf{v}_0^M}, \mathbf{B})$.

The observation error covariance matrix, \mathbf{R} , is also an unknown quantity in solar wind modelling. Properly addressing this is a substantial research topic in its own right [*Owens et al.*, 2020b]. In addition to the measurement uncertainty, \mathbf{y} , it also accounts for the uncertainty from the “representativity” error [*Janjić et al.*, 2017], that includes the errors due to approximating a continuous process in discrete space, from representing an observation in the incorrect location, and from representing a single measurement over the (potentially large) volume of a grid-cell (amongst others). Additionally, there is also an implicit component of the model error hidden within $\mathcal{H}(\mathbf{x})$ which further complicates the specification of this quantity. As in *Lang and Owens* [2019], we specify the observation error covariance matrix as a diagonal matrix (i.e. assuming that the observations are independent of one another) with standard deviation approximated as 10% of the mean prior solar wind speed at the observation radius. This is a somewhat arbitrary value, as the true \mathbf{R} matrix will include a term that varies depending upon the observation’s latitude offset from Earth and phase of solar cycle, etc, but it provides a starting point from which we can progress and test such assumptions. This gives:

$$\begin{aligned}
 R_{kk} &= (0.1 \overline{\mathbf{v}_{\mathbf{r}_k}^b})^2 \\
 &= (0.1 \sum_{i=1}^{N_\phi} [v_r^b(\phi_i)])^2,
 \end{aligned} \tag{7}$$

Observation location	Prior	Posterior	STEREO B Fc
STEREO A	114.507 ± 8.618	80.419 ± 5.626	N/A
STEREO B	115.965 ± 9.111	79.384 ± 5.870	N/A
ACE	113.349 ± 8.416	76.089 ± 5.387	77.752 ± 5.951
All avg.	114.607 ± 8.715	78.631 ± 5.628	N/A

Table 1: Table showing mean RMSEs \pm their standard errors for the prior, posterior and STEREO B forecasts at each observation location over the whole 7 year window.

where $0 \leq k \leq N_y$ is the observation number and $N_\phi = 128$ is the number of longitude points.

The BRaVDA scheme is run with these parameters for consecutive 27-day windows (each approximating 1 solar rotation from Earth’s perspective) spanning the 7-year operational window of STEREO B, assimilating all available observations from *STEREOA*, *STEREOB* and *ACE*. This produces initial conditions for forecasting the next 27-day period. The HUXt model is used to produce the forecast for the next 27-day window, with no additional observational constraints. This is summarised in Figure 3.

5 Results

5.1 Forecasting results over the whole 7–year period

This section describes the results of the forecasts produced using the data assimilation over the whole 7-year window. As mentioned in the previous sections, 27 day forecasts of the solar wind are produced for the prior state (generated from an ensemble of MAS runs) and the posterior state (the resultant solar wind from the DA). At ACE, we also compared against the STEREO B corotation forecast. This involves time-shifting STEREO B observations by Δt , given by:

$$\Delta t = \frac{\Delta\phi_B}{\Omega_{ROT}} \quad (8)$$

where $\Delta\phi_B$ is the longitude difference between STEREO B and Earth. See *Thomas et al.* [2018]; *Kohutova et al.* [2016] for more details.

For each 27-day forecast window, Root Mean Squared Error (RMSE) is computed over the whole 27-day forecast window, i.e.:

$$RMSE_{27,y} = \sqrt{\frac{1}{N_y} \sum_{i=1}^{N_y} [(y_i - x_i)^2]} \quad (9)$$

where N_y corresponds to the number of STEREO A, B or ACE observations during the 27-day forecast window, y_i correspond to the STEREO A, B or ACE observations and the x_i are the prior/posterior state, at the relevant satellite’s time/location.

This measures the accuracy of the solar wind forecasts are over the whole 27-day forecast window. RMSE is a simple point-by-point analysis, which can be problematic

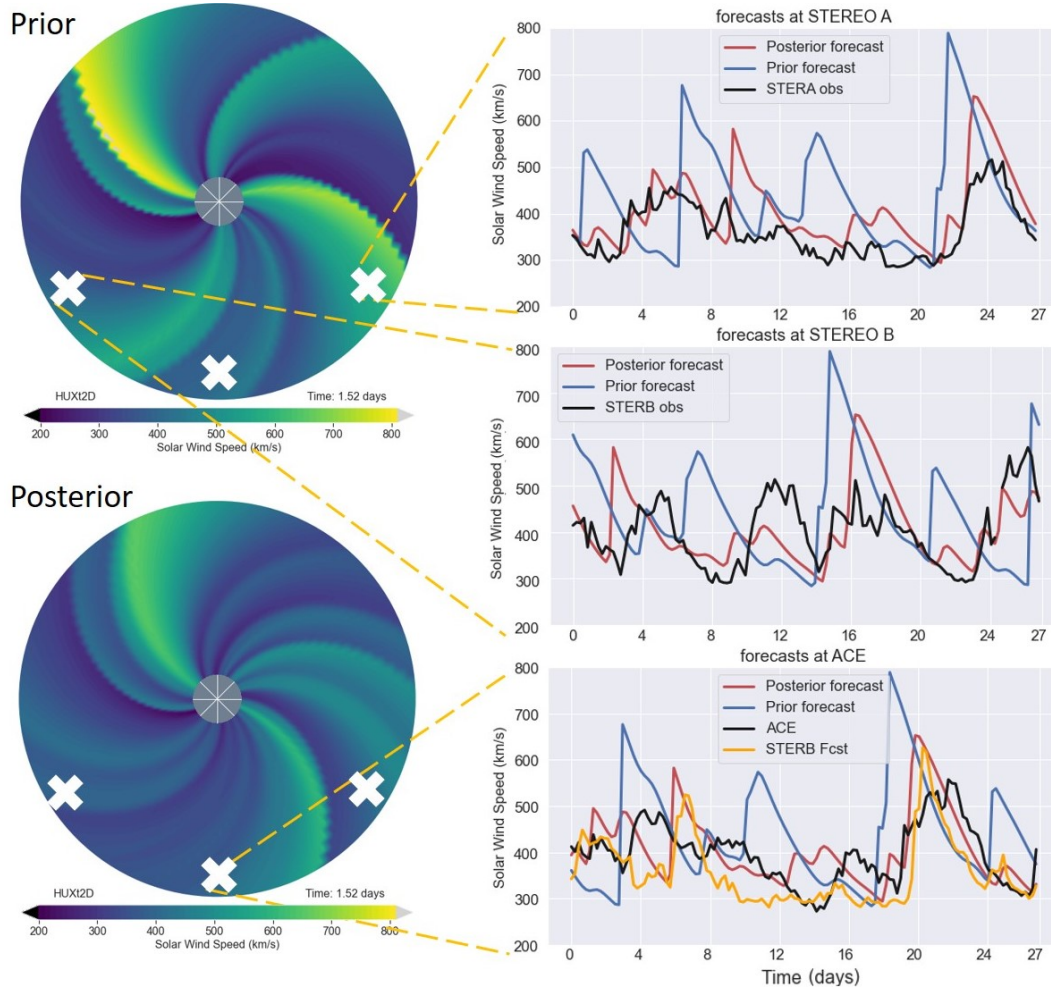


Figure 4: Schematic showcasing prior (no-DA) and posterior (DA) simulations using the HUXt model on the left hand side. The approximate locations of STEREO B, ACE and STEREO A are marked with white crosses (left, middle and right respectively) on the simulations. On the right of the schematic are the solar wind speeds observed at STEREO A (top), STEREO B (middle) and ACE(bottom), along with the prior (blue) and posterior (red) HUXt solar wind estimates at the respective satellites. At ACE, the corotation forecast from STEREO-B is also plotted (orange).

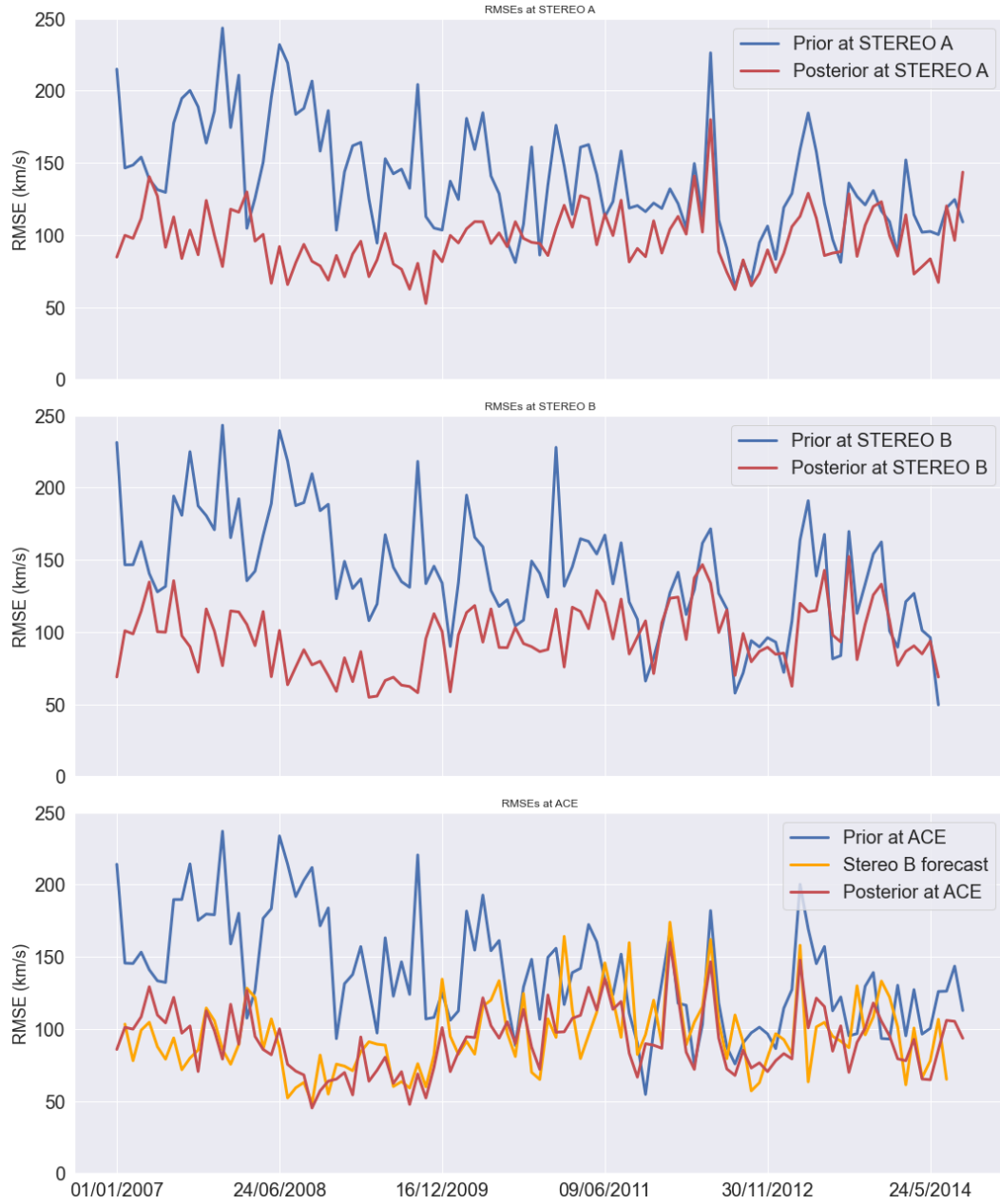


Figure 5: Root mean-square error (RMSE) of the solar wind speed averaged over each 27 day window. The top row gives the RMSEs at STEREO A, the middle row gives the RMSEs at STEREO B and the bottom row gives the RMSEs at ACE. The blue lines indicate the prior (no DA) forecast RMSEs, the red lines indicate the posterior (DA) forecast RMSEs and the orange line on the bottom plot gives the STEREO B corotation forecast at ACE.

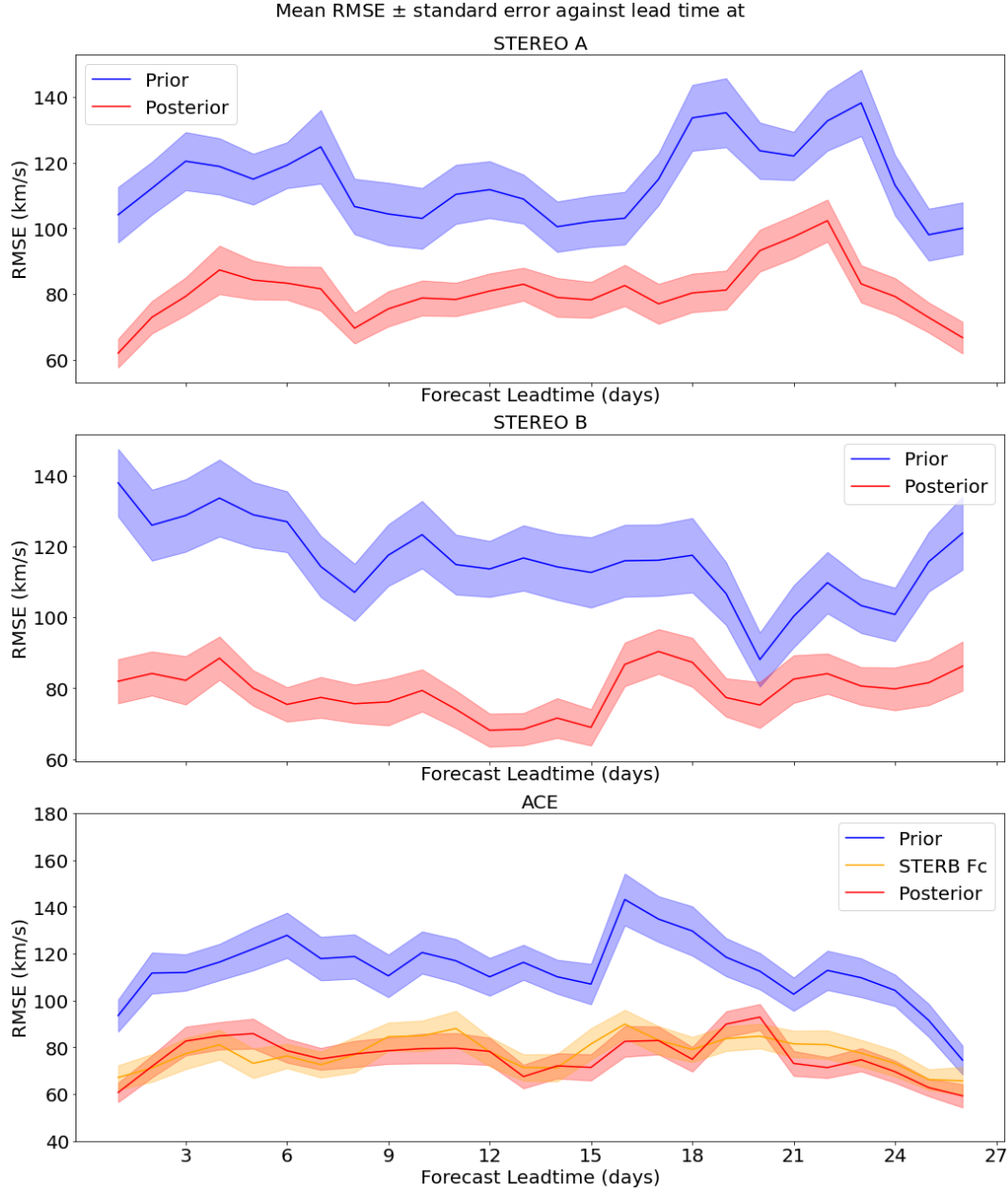


Figure 6: The mean forecast RMSEs of the solar wind speed plotted against forecast lead-time. The top row corresponds to the RMSEs at STEREO A, the middle row corresponds to the RMSEs at STEREO B and the bottom row corresponds the RMSEs at ACE. The blue lines indicate the prior (no DA) forecast RMSEs, the solid red lines indicate the posterior (DA) forecast RMSEs and the solid orange line on the bottom plot gives the STEREO B corotation forecast at ACE. The solid lines indicate mean RMSEs while the shaded regions span one standard error.

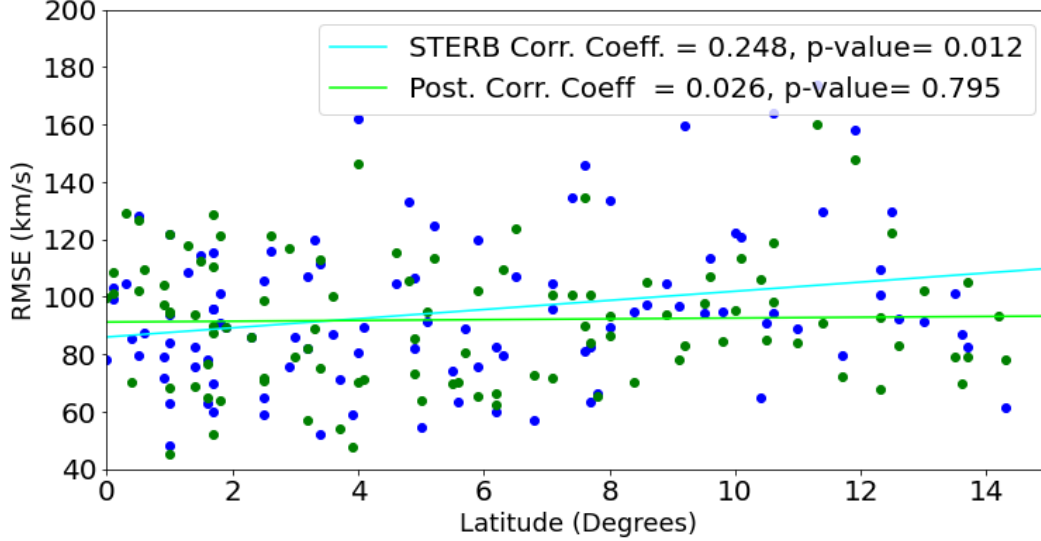


Figure 7: The 27-day forecast RMSEs of the solar wind speed plotted against the absolute difference between STEREO B and ACE’s latitude for the entire 7-year period. The blue points correspond to the STEREO B corotation forecast and the green points relate to the DA posterior forecast. The blue and green lines represent the line of best-fit for the corotation and posterior forecasts respectively. The Pearson’s product-moment correlation coefficient indicating the strength of the correlation between the data and the line of best-fit, along with its associated p-value, is given in the legend.

for distinguishing between forecasts with insufficient variability and forecasts with small timing errors in events [Owens, 2018]. However, in this particular application, it nevertheless provides a useful initial diagnostic of performance. More detailed forecast validation will be the subject of future research.

Figure 5 shows the 27-day forecast RMSEs against time. The posterior forecast RMSEs are lower than the prior forecasts RMSEs for the vast majority of windows, at all spacecraft locations. This result indicates that the improvements made by the DA in the assimilation window are carried into the forecast window by the HUXt model.

In the first half of the 7-year period (i.e., before 2011), we note that the prior state has relatively high RMSEs. This is likely due to the Sun being in the solar minimum phase, meaning that there is greater representivity errors due to latitudinal offsets are observed (see ? for more details). We can see that the data assimilation is able to produce more accurate solar wind speed forecasts at all observation locations throughout this time period.

In the latter half of the 7 year period, the solar maximum phase implies the prior state has lower RMSEs due to reduced latitudinal representivity errors and lower solar wind speed [?]. In addition, solar maximum is associated with more transient events. These facts lead to a reduction in the improvement in forecast RMSEs from the posterior forecast (as the HUXt forecasts here assume the Sun is in steady-state). Nonetheless, the DA still leads to improvements in the forecast solar wind speeds in comparison to the prior forecasts.

At ACE, we also compare the DA posterior state to the corotation forecast from STEREO B. The two forecasts are comparable when looking at the 27-day forecast

RMSE. This is to be expected somewhat, as the data assimilation analysis incorporates the observation at STEREO B within it. Nonetheless, the posterior forecast at ACE has lower 27-day RMSEs for 63 out of 105 windows (that is, the posterior forecasts are better for 60% of windows). Note that STEREO B forecast does not exist for three windows, due to insufficient observations (but the DA posterior forecast still exists, as it can be based on ACE and STEREO A data).

Figure 6 shows the mean forecast RMSEs as a function of forecast lead-time at STEREO A, STEREO B and ACE. The mean RMSE for each forecast lead-time (in days) is calculated as:

$$RMSE_{t,y} = \sqrt{\frac{1}{N_w} \frac{1}{N_t} \sum_{i=1}^{N_w} \sum_{j=s_t}^{e_t} [(y_{i,j} - x_{i,j})^2]} \quad (10)$$

where N_w is the number of 27-day windows (105 in total), $N_t = e_t - s_t$ is the number of observations during the t^{th} day, $y_{i,j}$ is the j^{th} observation in the i^{th} 27-day window and $x_{i,j}$ is the state corresponding to $y_{i,j}$.

At all observation locations, the posterior solar wind speed forecast has lower mean RMSE than the prior solar wind speed forecast for all lead-times by about 40 – 50 km/s. It can also be seen that the standard error for the posterior state is smaller than the prior for all observation locations and lead-times. At ACE, the STEREO B corotation forecast RMSE is very similar to the posterior forecast RMSE over all lead-times. However the posterior forecast does have a slightly lower mean RMSE (see Table 1) and standard error than the STEREO B forecast. Furthermore, the mean posterior forecast RMSE is lower for 16 lead-times out of 27 considered (60%).

The distribution of RMSEs for the STEREO-B corotation forecast as a function of the absolute heliographic latitude difference between STEREO B and ACE/Earth shows a positive correlation (with a gradient of $1.593 \text{ km s}^{-1} \text{ deg}^{-1}$). This is somewhat expected ([Owens *et al.*, 2020b]) and will be explored in more detail later in the study. Furthermore, the p-value indicates that this correlation is significant at the 95% confidence level. As the latitude difference between STEREO B and ACE becomes greater, the STEREO B observations are sampling the solar wind in different regions of the Sun (eg. spacecraft could be sampling solar wind from different coronal holes). The posterior forecast does not display this correlation, the p-value indicating that the correlation found is nonsignificant and the line of best-fit being a flat line (gradient of posterior line of best fit is $0.138 \text{ km s}^{-1} \text{ deg}^{-1}$). This means that when STEREO B and ACE are at different latitudes, the data assimilation is able to remove this systematic error through combination with the other observation sources (ACE and STEREO A). However, this does also work against the posterior forecast, as it does not necessarily lead to improvements over the STEREO B corotation forecast when the latitude differences are small. This could be due to STEREO A being at a larger latitude offset from ACE ‘pulling’ the posterior forecast away from the ACE data.

In the next sections, we shall investigate how the data assimilation performs in different solar cycle regimes and where the DA can give the greatest improvements when compared to the STEREO B forecast.

5.2 Forecasting the solar wind speed during different solar cycle phases

The solar activity is expected to influence the forecasting skill of both the DA and corotation forecasts. During solar maximum there is an increased number of transient events, such as coronal mass ejections (CMEs), and a more rapidly evolving solar wind structure. Conversely, solar minimum results in fewer transients and a more slowly evolving solar wind structure. Solar wind speed is highly structured in latitude at this

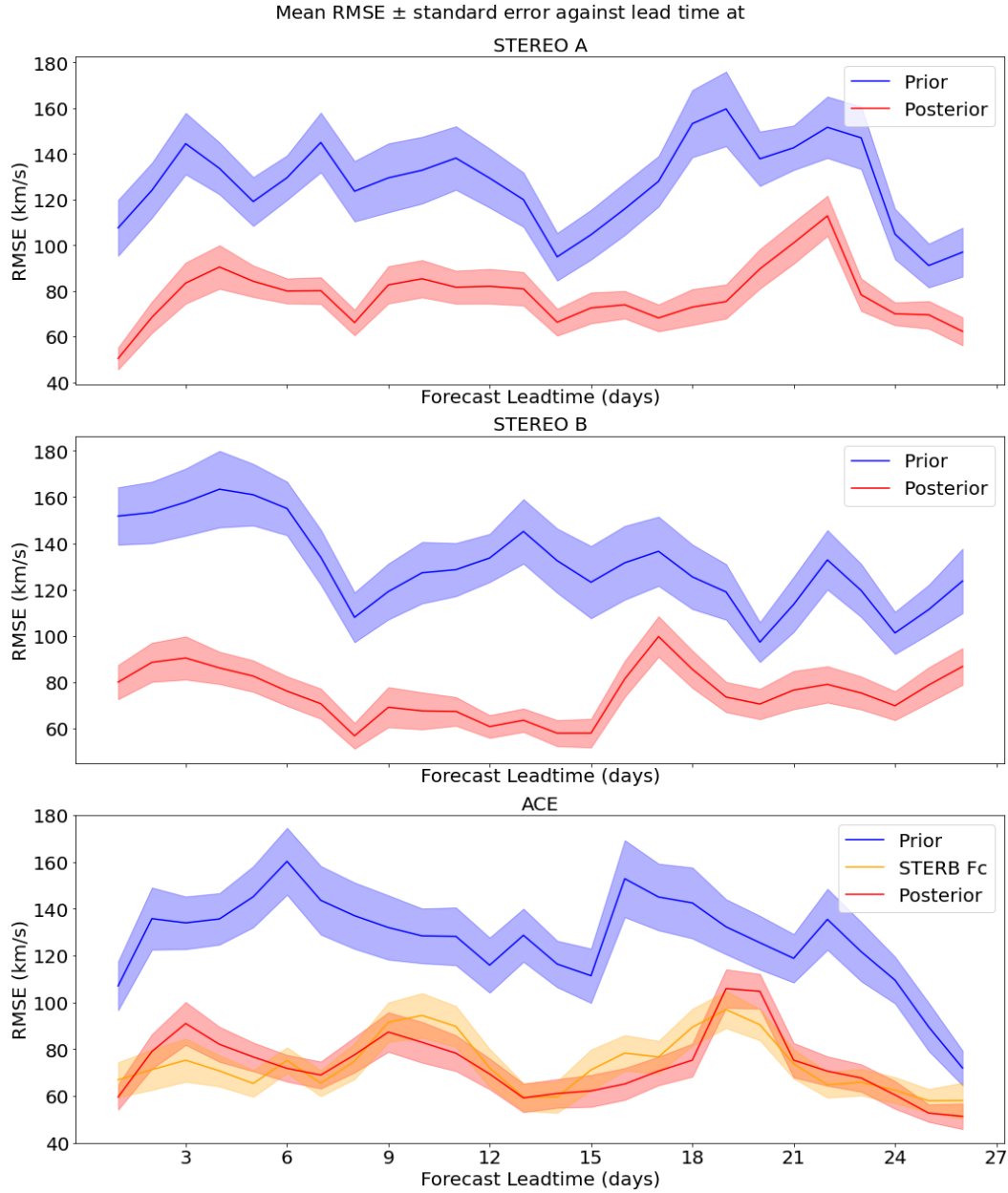


Figure 8: The mean forecast RMSEs of the solar wind speed plotted against lead-time during solar minimum ($sC < 0.2$ or $sC \geq 0.7$). The top row corresponds to the RMSEs at STEREO A, the middle row corresponds to the RMSEs at STEREO B and the bottom row corresponds to the RMSEs at ACE. The blue lines indicate the prior (no DA) forecast RMSEs, the red lines indicate the posterior (DA) forecast RMSEs and the orange line on the bottom plot gives the STEREO B corotation forecast at ACE. The shaded regions indicate one standard error around the mean.

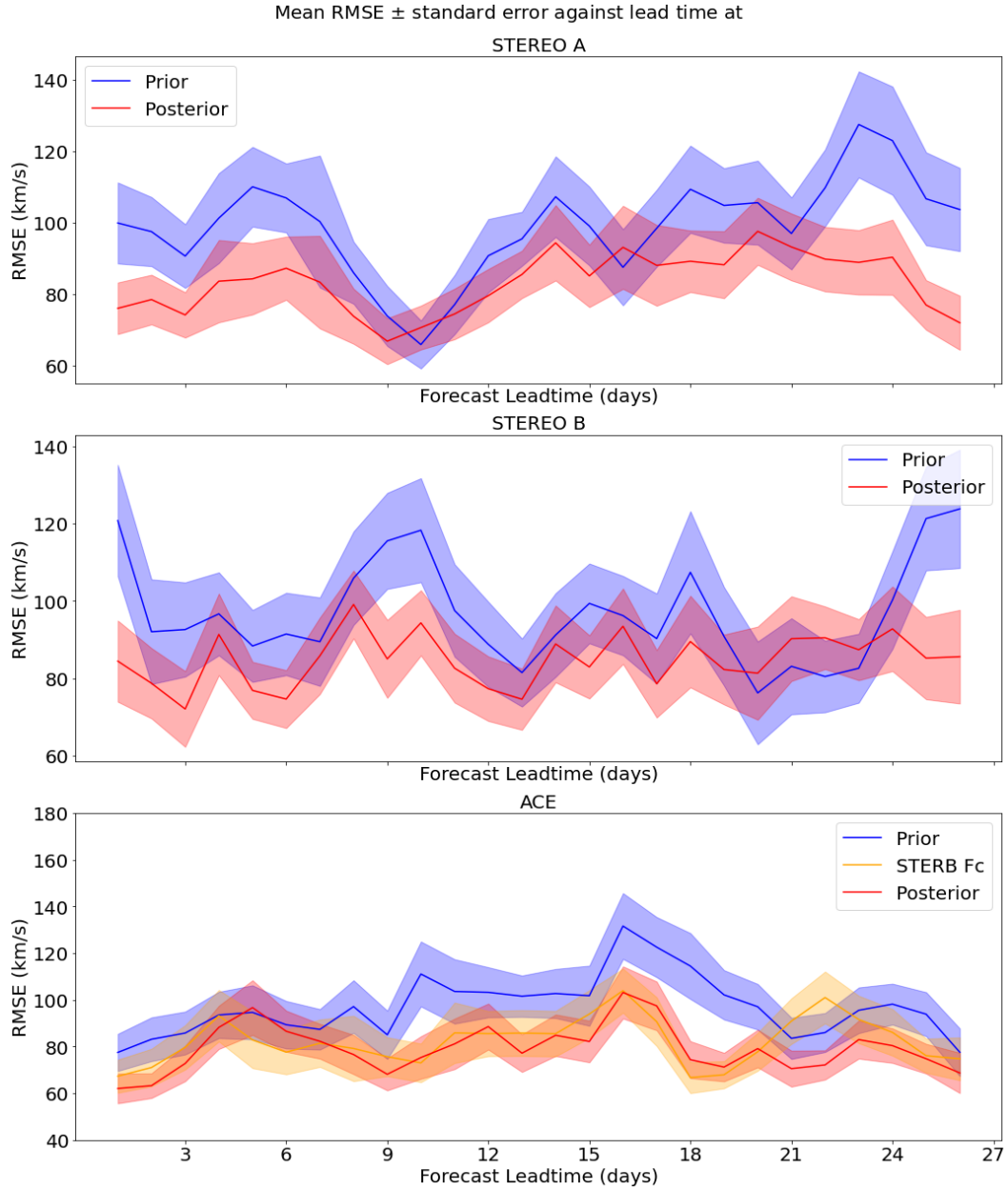


Figure 9: The mean forecast RMSEs of the solar wind speed plotted against lead-time during solar maximum ($0.2 \leq sC < 0.7$). The top row corresponds to the RMSEs at STEREO A, the middle row corresponds to the RMSEs at STEREO B and the bottom row corresponds to the RMSEs at ACE. The blue lines indicate the prior (no DA) forecast RMSEs, the solid red lines indicate the posterior (DA) forecast RMSEs and the solid orange line on the bottom plot gives the STEREO B corotation forecast at ACE. The shaded regions span one standard error about the mean.

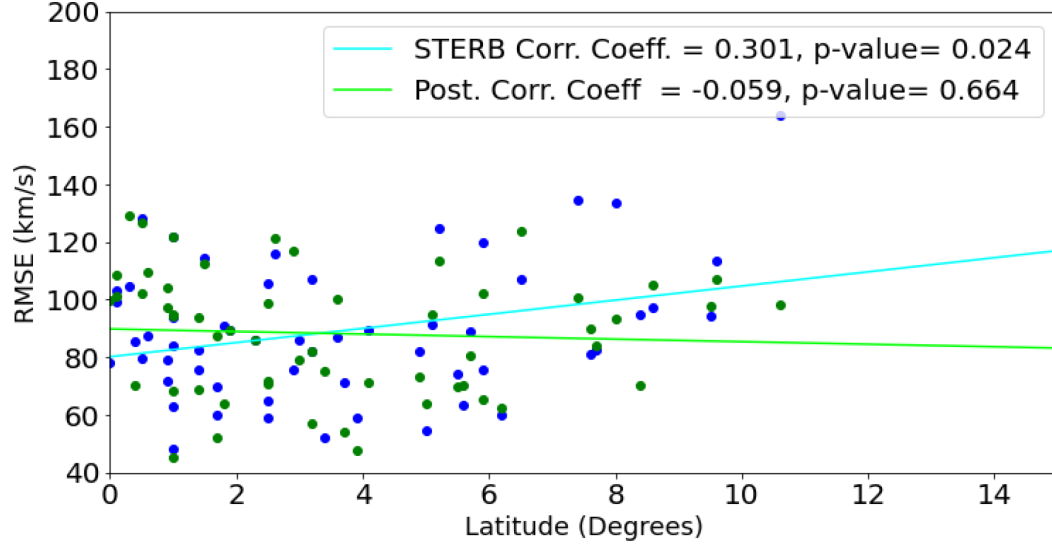
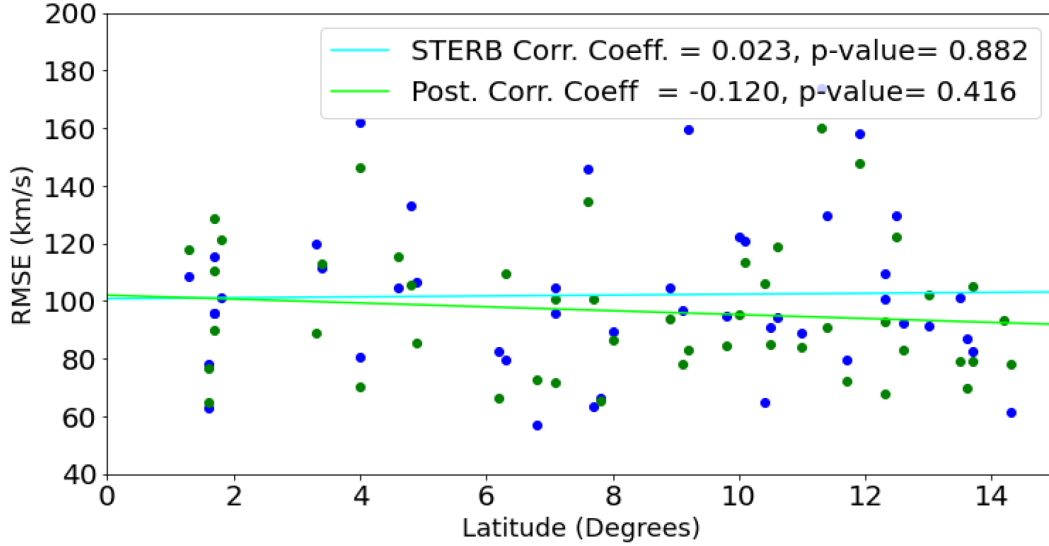
(a) Solar minimum ($sC < 0.2$ or $sC \geq 0.7$)(b) Solar maximum ($0.2 \leq sC < 0.7$)

Figure 10: The 27-day forecast RMSEs of the solar wind speed plotted against the absolute difference between STEREO B and ACE's latitude during solar minimum (top panel) and solar maximum (bottom panel). The blue points correspond to the STEREO B corotation forecast and the green points relate to the posterior forecast. The blue and green lines represent the line of best-fit for the corotation and posterior forecasts, respectively. The Pearson's product-moment correlation coefficient indicating the strength of the correlation between the data and the line of best-fit, along with its associated p-value, is given in the legend.

Observation location	Prior	Posterior	STEREO B Fc
STEREO A	127.146 ± 12.270	78.056 ± 7.039	N/A
STEREO B	131.010 ± 12.712	75.096 ± 7.106	N/A
ACE	127.145 ± 12.209	73.386 ± 6.737	73.802 ± 7.122
All avg.	128.434 ± 12.397	75.513 ± 6.961	N/A

Table 2: Table showing mean RMSEs \pm their standard errors for the prior, posterior and STEREO B forecasts at each observation location during solar minimum.

Observation location	Prior	Posterior	STEREO B Fc
STEREO A	99.057 ± 10.961	83.287 ± 8.732	N/A
STEREO B	96.992 ± 11.893	84.806 ± 9.521	N/A
ACE	96.967 ± 10.610	79.291 ± 8.294	82.541 ± 9.554
All avg.	97.672 ± 11.155	82.461 ± 8.849	N/A

Table 3: Table showing mean RMSEs \pm their standard errors for the prior, posterior and STEREO B forecasts at each observation location during solar maximum.

time. The solar cycle (from one solar minimum to the next) is approximately 11 years. In this section, we denote the phase of the solar cycle as $s_C \in [0, 1]$. 0 denotes the start of the solar cycle (at solar minimum), 1 denotes the end of the solar cycle (at solar minimum) and 0.5 is the mid-point of the solar cycle. Solar maximum typically occurs prior to $s_C = 0.5$.

We split forecasts of the solar wind speed into two groups: those around solar minimum ($s_C \geq 0.7$ or $s_C < 0.2$) and those forecast around solar maximum ($0.2 \leq s_C < 0.7$). In this way, we can diagnose how the solar wind forecasts behave during these two regimes of the solar cycle. Unfortunately, however, this will not be a like-for-like comparison as the STEREO B spacecraft is moving away from Earth at a rate of $22.5^\circ/\text{yr}$, this means that the corotation forecasts produced later in the 7-year period (i.e. during the solar maximum phase) will be of longer lead-time than those produced earlier. This means that we would expect the RMSEs to be larger during the solar maximum phase than those in solar minimum, due to the fact that they occur when STEREO B is further away and hence forecasts have a longer lead-time. This is in addition to the more rapidly evolving solar wind structure and increased number of solar wind transients at solar maximum.

The 7-years that we have STEREO B observations and have run these solar wind speed forecasts, from 2007 – 2014, coincide with the end of Solar Cycle 23 (> 0.84) and the first half of Solar Cycle 24 (< 0.51). This means that we have far more forecasts occurring around solar minimum than those around solar maximum.

Tables 2 and 3 show that during the solar minimum regime, the prior solar wind speed RMSEs and uncertainties are greater than during the solar maximum regime, as seen in the previous time series plots. During solar minimum the posterior forecast and the STEREO B corotation forecast show a greater improvement over the prior state and greater reduction in uncertainty.

Figure 8 shows that during solar minimum, the posterior and the STEREO B corotation forecasts show a very similar RMSE pattern for all lead-times, with a mean RMSE difference of 0.086km/s over all lead-times. Nonetheless, during the solar minimum, the mean posterior forecast RMSEs are lower than the STEREO B corotation forecast RMSEs for 17 considered lead-times out of 27. During solar maximum (see Figure 9), however, the STEREO B corotation forecast mean RMSE is higher than the posterior forecast RMSE between 20 and 23 days (by an average of 17.393km/s) and with greater uncertainty (mean standard deviation is 13.95km/s during this period). Despite this large difference in mean RMSEs, the mean STEREO B corotation forecasts are better than the posterior forecasts for 11 of the 27 lead-time days. On the whole, Figures 8 and 9 show that the STEREO B corotation forecast and the posterior forecast RMSEs are broadly similar during solar minimum and maximum, exhibiting similar means and uncertainty patterns.

By contrast, Figure 10 shows a very different picture of forecasting skill as a function of latitude offset during solar minimum and solar maximum. Figure 10a) shows the 27 day RMSEs of the STEREO B corotation forecast against the posterior forecasts during solar minimum. It can be seen that there is a significant (at the 95% confidence level) positive correlation between STEREO B corotation forecast RMSEs and STEREO B's latitude difference from Earth during solar minimum (with gradient of $3.078\text{kms}^{-1}\text{deg}^{-1}$). By comparison, during solar maximum, despite STEREO B reaching a greater latitude offset from ACE, the STEREO B corotation forecast RMSE is uncorrelated with the latitude offset of STEREO B (in fact, the line of best-fit's gradient is $-0.013\text{kms}^{-1}\text{deg}^{-1}$ and is nonsignificantly anti-correlated with latitude). The reason for this almost counter-intuitive result can be explained by looking at the solar wind structure during solar minimum and solar maximum *Owens et al.* [2020b]. During solar minimum, the slow wind band (and heliospheric current sheet) is closely

aligned with the heliographic equator ($\pm 20^\circ$), this means that for a relatively small change in latitude, large deviations in solar wind behaviour are observed. Therefore, during solar minimum it is more likely that when STEREO B is more latitudinally offset from ACE, it will also be more offset with respect to solar wind structure. In comparison, during solar maximum, slow wind extends to high latitude. This means that there are generally smaller gradients of solar wind structure with latitude, hence STEREO B and ACE are more likely to be observing the same solar wind behaviour despite their latitudinal offset. For more details on this phenomena, see *Owens et al.* [2020b].

Reassuringly, the data assimilation is able to remove this latitudinal correlation and produce a more consistent forecast for all latitudinal offsets between STEREO B and ACE. It can be seen that during solar minimum, when this effect is greatest, the posterior forecast's line of best fit is almost flat (its gradient is $0.315 \text{ km s}^{-1} \text{ deg}^{-1}$) with very little, nonsignificant correlation. As noted before in the plot of latitudinal offset against RMSE for all the data, this does mean that higher RMSE can be observed for the posterior forecasts when STEREO B's latitude is close to that of Earth. This further illustrates the need to investigate and incorporate the latitudinal representivity into the observation error covariance matrix when performing the data assimilation. During the solar maximum, the posterior is barely correlated with the latitudinal offset, nonetheless, it can be seen that there is a consistent reduction in posterior forecast RMSE when compared to the STEREO B corotation forecast.

6 Discussion and Conclusions

The experiments shown in this study illustrate how data assimilation can be used to produce superior forecasts of the solar wind up to one solar rotation (27 days) ahead.

Over the whole 7-year period of study, we see that the data assimilation scheme (BRaVDA) is able to improve forecasts of the solar wind speed when compared to the prior ensemble, reducing RMSE by an average of 36 km/s at all spacecraft considered. During solar maximum, this improvement in forecast RMSE is reduced to about 14 km/s , but during solar minimum solar, this is increased to about 48 km/s . This shows that the application of data assimilation, even with a relatively simple solar wind model, can lead to large improvements in forecasting accuracy.

Additionally, the uncertainties present in the forecast estimates are greatly reduced by assimilating data. This decrease was on average by $30 - 40 \text{ km/s}$ lower than the prior forecast RMSE standard deviation, which means that we can have increased confidence in the forecasts produced when using data assimilation.

The data assimilation forecasts at Earth are of similar accuracy and uncertainty to STEREO B's corotation forecast accuracy and uncertainty. This is somewhat to be expected as the data assimilation is also based upon the STEREO B observation and is expected to recreate it at the satellite location. But the DA approach is advantageous for two reasons. Firstly, the data assimilation scheme provides far more information than the STEREO B corotation forecast. Whilst corotation gives us a point forecast at Earth (or can be corotated to any other point at the same latitude and heliocentric distance), the DA scheme maps observational data throughout the model domain. This means that the DA scheme is able to give us improved estimates of the solar wind throughout the inner heliosphere. The advantage of this is that this will give a more accurate representation of the solar wind between the Sun and Earth, which will provide a more suitable medium for CMEs to be propagated through (e.g., see *Owens et al.* [2020a]; ?). This will be elaborated upon more in a later study.

Secondly, the data assimilation also provides a more consistent and robust forecast for the solar wind compared to the STEREO B forecast. DA is able to reduce the representivity errors that are caused by the latitudinal offset between STEREO B and ACE/Earth. The STEREO B corotation forecast is sensitive to the latitudinal offset between STEREO B and Earth, with poorer forecasts occurring when STEREO B is at greater latitudes. This is restricted to solar minimum, when there are greatly differing solar wind regimes at different latitudes. By relying on more than one observation source and accounting for potential errors in the observations, data assimilation is able to compensate for these errors and remove the correlation between forecast error and latitude offset. The DA scheme will also reduce the effect of transient structures (such as coronal mass ejections) seen only at STEREO B, thus reducing false positive forecasts of high-speed streams. More study is required to determine how to balance the representivity errors contributed from latitudinal offset and the "age" of observations for the purposes of forecasting at Earth. Both of these effects are expected to have competing solar cycle variations.

The major outstanding issue with using a variational data assimilation scheme in an operational setting is that the adjoint method is not scalable to higher-dimensional or more complex models. The tangent linear and adjoint models are unique to each numerical model and can be extremely difficult and require many human-years to create an efficient scheme (however, once created, the adjoint method is an extremely powerful and efficient tool, as shown in this paper). This means that without substantial investment, it will not be possible to utilise an adjoint model in a full MHD model, such as Enlil or EUHFORIA. This issue indicates that it is perhaps more useful to use the adjoint-based data assimilation methods with smaller, simpler solar wind/MHD models. Indeed, HUXt was originally intended as a surrogate model for more complex MHD models. Thus BRaVDA could be used to define an optimum set of boundary conditions using solar wind observations which can then be used to drive more complex models. For DA within more complex MHD models, in order to map observational information from near-Earth space to the inner-boundary, it is perhaps more useful to use a hybrid data assimilation method, such as Ensemble-4DVar [Amezcuca *et al.*, 2017; Goodliff *et al.*, 2017], or a smoother-based data assimilation method, such as the Iterative Ensemble Kalman Smoother [Bocquet and Sakov, 2014]. These will be tested in future studies.

Acknowledgments

We are grateful to the Space Physics Data Facility and National Space Science Data Center for OMNI. MAS model output is available from the Predictive Science Inc. website: (<http://www.predsci.com/mhdweb/home.php>). Work was part-funded by Science and Technology Facilities Council (STFC) grant number ST/R000921/1, and Natural Environment Research Council (NERC) grant number NE/P016928/1. Jake Witherington was funded by a RAS undergraduate bursary. Harriet Turner is funded through SCENARIO grant number NE/S007261/1. HUXt can be downloaded in the Python programming language from <https://github.com/University-of-Reading-Space-Science/HUXt>. BRaVDA can be downloaded in the Python programming language from <https://github.com/University-of-Reading-Space-Science/BRaVDA>.

References

- Amezcuca, J., M. Goodliff, and P. J. Van Leeuwen (2017), A weak-constraint 4D EnsembleVar. Part I: formulation and simple model experiments, *Tellus A: Dynamic Meteorology and Oceanography*, 69(1), 1271,564, doi:10.1080/16000870.2016.1271564.
- Arge, C. N., D. Odstrcil, V. J. Pizzo, and L. R. Mayer (2003), Improved Method for Specifying Solar Wind Speed Near the Sun, in *AIP Conference Proceedings*, vol. 679, pp. 190–193, American Institute of Physics Inc., doi:10.1063/1.1618574.

- Arge, C. N., C. J. Henney, J. Koller, C. R. Compeau, S. Young, D. MacKenzie, A. Fay, J. W. Harvey, M. Maksimovic, K. Issautier, N. Meyer-Vernet, M. Moncuquet, and F. Pantellini (2010), Air Force Data Assimilative Photospheric Flux Transport (ADAPT) Model, in *AIP Conference Proceedings*, vol. 1216, pp. 343–346, American Institute of Physics, doi:10.1063/1.3395870.
- Bocquet, M., and P. Sakov (2014), An iterative ensemble Kalman smoother, *Quarterly Journal of the Royal Meteorological Society*, *140*(682), 1521–1535, doi:10.1002/qj.2236.
- Breen, A. R., R. A. Fallows, M. M. Bisi, P. Thomasson, C. A. Jordan, G. Wannberg, and R. A. Jones (2006), Extremely long baseline interplanetary scintillation measurements of solar wind velocity, *Journal of Geophysical Research*, *111*(A8), A08,104, doi:10.1029/2005JA011485.
- Browne, P. A., and S. Wilson (2015), A simple method for integrating a complex model into an ensemble data assimilation system using MPI, *Environmental Modelling & Software*, *68*, 122–128.
- Bust, G. S., and C. N. Mitchell (2008), History, current state, and future directions of ionospheric imaging, *Reviews of Geophysics*, *46*(1), RG1003, doi:10.1029/2006RG000212.
- Durazo, J. A., E. J. Kostelich, and A. Mahalov (2017), Local ensemble transform Kalman filter for ionospheric data assimilation: Observation influence analysis during a geomagnetic storm event, *Journal of Geophysical Research: Space Physics*, *122*(9), 9652–9669, doi:10.1002/2017JA024274.
- Evensen, G., D. P. Dee, and J. Schröter (1998), Parameter estimation in dynamical models, in *Ocean Modeling and Parameterization*, pp. 373–398, Springer.
- Eyles, C. J., R. A. Harrison, C. J. Davis, N. R. Waltham, B. M. Shaughnessy, H. C. A. Mapson-Menard, D. Bewsher, S. R. Crothers, J. A. Davies, G. M. Simnett, R. A. Howard, J. D. Moses, J. S. Newmark, D. G. Socker, J.-P. Halain, J.-M. Defise, E. Mazy, and P. Rochus (2009), The Heliospheric Imagers Onboard the STEREO Mission, *Solar Physics*, *254*(2), 387–445, doi:10.1007/s11207-008-9299-0.
- Goodliff, M., J. Amezcua, and P. J. Van Leeuwen (2017), A weak-constraint 4DensemblesVar. Part II: experiments with larger models, *Tellus A: Dynamic Meteorology and Oceanography*, *69*(1), 1271,565, doi:10.1080/16000870.2016.1271565.
- Hapgood, M. A. (2011), Towards a scientific understanding of the risk from extreme space weather, *Advances in Space Research*, *47*(12), 2059–2072, doi:10.1016/j.asr.2010.02.007.
- Janjić, T., N. Bormann, M. Bocquet, J. A. Carton, S. E. Cohn, S. L. Dance, S. N. Losa, N. K. Nichols, R. Potthast, J. A. Waller, and P. Weston (2017), On the representation error in data assimilation, *Quarterly Journal of the Royal Meteorological Society*, doi:10.1002/qj.3130.
- Kaiser, M. L., T. A. Kucera, J. M. Davila, O. C. S. Cyr, M. Guhathakurta, and E. Christian (2008), The STEREO mission: An introduction, in *The STEREO Mission*, pp. 5–16, Springer.
- Kalnay, E. (2003), *Atmospheric modeling, data assimilation and predictability*, Cambridge university press.
- Kohutova, P., F.-X. Bocquet, E. M. Henley, and M. J. Owens (2016), Improving solar wind persistence forecasts: Removing transient space weather events, and using observations away from the Sun-Earth line, *Space Weather*, *14*(10), 802–818, doi:10.1002/2016SW001447.
- Lang, M., and M. J. Owens (2019), A Variational Approach to Data Assimilation in the Solar Wind, *Space Weather*, *17*(1), 59–83, doi:10.1029/2018SW001857.
- Lang, M., P. J. van Leeuwen, and P. A. Browne (2016), A systematic method of parameterisation estimation using data assimilation, *Tellus A*, *68*(0).
- Lang, M., P. Browne, P. J. van Leeuwen, and M. Owens (2017), Data Assimilation in the Solar Wind: Challenges and First Results, *Space Weather*, *15*(11), 1490–1510,

- doi:10.1002/2017SW001681.
- Linker, J. A., Z. Mikić, D. A. Biesecker, R. J. Forsyth, S. E. Gibson, A. J. Lazarus, A. Lecinski, P. Riley, A. Szabo, and B. J. Thompson (1999), Magnetohydrodynamic modeling of the solar corona during Whole Sun Month, *Journal of Geophysical Research: Space Physics*, *104*(A5), 9809–9830, doi:10.1029/1998JA900159.
- Mackay, D., and A. Yeates (2012), The Sun’s Global Photospheric and Coronal Magnetic Fields: Observations and Models, *Living Reviews in Solar Physics*, *9*(1), 6, doi:10.12942/lrsp-2012-6.
- McGregor, S. L., W. J. Hughes, C. N. Arge, M. J. Owens, and D. Odstrcil (2011), The distribution of solar wind speeds during solar minimum: Calibration for numerical solar wind modeling constraints on the source of the slow solar wind, *Journal of Geophysical Research: Space Physics*, *116*(A3), doi:10.1029/2010JA015881.
- Nerger, L., W. Hiller, and J. Schröter (2005), PDAF-the parallel data assimilation framework: experiences with Kalman filtering, in *Use of high performance computing in meteorology: proceedings of the Eleventh ECMWF Workshop on the Use of High Performance Computing in Meteorology, Reading, UK, 25-29 October 2004/Eds.: Walter Zwiefelhofer; Geoge Mozdzynski, Singapore [ua]: World*, pp. 63–83.
- Odstrcil, D. (2003), Modeling 3-D solar wind structure, *Advances in Space Research*, *32*(4), 497–506.
- Owens, M., M. Lang, L. Barnard, P. Riley, M. Ben-Nun, C. J. Scott, M. Lockwood, M. A. Reiss, C. N. Arge, and S. Gonzi (2020a), A Computationally Efficient, Time-Dependent Model of the Solar Wind for Use as a Surrogate to Three-Dimensional Numerical Magnetohydrodynamic Simulations, *Solar Physics*, *295*(3), 43, doi:10.1007/s11207-020-01605-3.
- Owens, M. J. (2018), Time-Window Approaches to Space-Weather Forecast Metrics: A Solar Wind Case Study, *Space Weather*, *16*(11), 1847–1861, doi:10.1029/2018SW002059.
- Owens, M. J., and R. J. Forsyth (2013), The heliospheric magnetic field, *Living Reviews in Solar Physics*, *10*(5), 5, doi:10.12942/lrsp-2013-5.
- Owens, M. J., and P. Riley (2017), Probabilistic Solar Wind Forecasting Using Large Ensembles of Near-Sun Conditions With a Simple One-Dimensional “Upwind” Scheme, *Space Weather*, *15*(11), 1461–1474, doi:10.1002/2017SW001679.
- Owens, M. J., M. Lang, P. Riley, M. Lockwood, and A. S. Lawless (2020b), Quantifying the latitudinal representivity of in situ solar wind observations, *Journal of Space Weather and Space Climate*, *10*, 8, doi:10.1051/swsc/2020009.
- Pereira, M. B., L. Berre, M. B. Pereira, and L. Berre (2006), The Use of an Ensemble Approach to Study the Background Error Covariances in a Global NWP Model, *Monthly Weather Review*, *134*(9), 2466–2489, doi:10.1175/MWR3189.1.
- Poedts, S., and J. Pomoell (2017), EUHFORIA: a solar wind and CME evolution model, *19th EGU General Assembly, EGU2017, proceedings from the conference held 23-28 April, 2017 in Vienna, Austria.*, p.7396, 19, 7396.
- Riley, P., and R. Lionello (2011), Mapping Solar Wind Streams from the Sun to 1 AU: A Comparison of Techniques, *Solar Physics*, *270*(2), 575–592, doi:10.1007/s11207-011-9766-x.
- Riley, P., J. A. Linker, R. Lionello, and Z. Mikic (2012), Corotating interaction regions during the recent solar minimum: The power and limitations of global MHD modeling, *Journal of Atmospheric and Solar-Terrestrial Physics*, *83*, 1–10, doi:10.1016/J.JASTP.2011.12.013.
- Riley, P., J. A. Linker, and C. N. Arge (2015), On the role played by magnetic expansion factor in the prediction of solar wind speed, *Space Weather*, *13*(3), 154–169, doi:10.1002/2014SW001144.
- Stone, E. C., A. M. Frandsen, R. A. Mewaldt, E. R. Christian, D. Margolies, J. F. Ormes, and F. Snow (1998), The advanced composition explorer, in *The Ad-*

- vanced Composition Explorer Mission*, vol. 86, pp. 1–22, Springer, doi:10.1023/A:1005082526237.
- Thomas, S. R., A. Fazakerley, R. T. Wicks, and L. Green (2018), Evaluating the Skill of Forecasts of the Near-Earth Solar Wind Using a Space Weather Monitor at L5, *Space Weather*, *16*(7), 814–828, doi:10.1029/2018SW001821.
- Wang, C., G. Hajj, X. Pi, I. G. Rosen, and B. Wilson (2004), Development of the Global Assimilative Ionospheric Model, *Radio Science*, *39*(1), doi:10.1029/2002RS002854.